

DEPARTMENT OF AEROSPACE ENGINEERING
COLLEGE OF ENGINEERING & TECHNOLOGY
OLD DOMINION UNIVERSITY
NORFOLK, VIRGINIA 23529

**MODELLING OF EDDY CURRENTS RELATED TO
LARGE ANGLE MAGNETIC SUSPENSION TEST FIXTURE**

By

Colin P. Britcher, Principal Investigator

and

Lucas E. Foster, Graduate Research Assistant

Final Report

For the period November 1, 1993 through October 31, 1994

Prepared for
National Aeronautics and Space Administration
Langley Research Center
Hampton, VA 23681-0001

Under
Research Grant NAG-1-1056
Nelson J. Groom, Technical Monitor
GCD-Spacecraft Controls Branch

**Submitted by the
Old Dominion University Research Foundation
P.O. Box 6369
Norfolk, VA 23508**



November 1994

MODELLING OF EDDY CURRENTS RELATED TO LARGE ANGLE MAGNETIC SUSPENSION TEST FIXTURE

Colin P. Britcher, Lucas E. Foster
Department of Aerospace Engineering
Old Dominion University
Norfolk, VA

SUMMARY

This report presents a preliminary analysis of the mathematical modelling of eddy current effects in a large-gap magnetic suspension system. It is shown that eddy currents can significantly affect the dynamic behaviour and control of these systems, but are amenable to measurement and modelling. A theoretical framework is presented, together with a comparison of computed and experimental data related to the Large Angle Magnetic Suspension Test Fixture at NASA Langley Research Center.

1.0 INTRODUCTION

In order to explore and develop technology required for the magnetic suspension of objects over large ranges of orientation, a small-scale laboratory development system, the Large Angle Magnetic Suspension Test Fixture (LAMSTF) has been constructed at NASA Langley Research Center. Possible applications for magnetic suspension systems of this general class include space payload pointing and manipulation, microgravity vibration isolation and wind tunnel model suspension [1]. An important objective of this particular project is to investigate the dynamic modelling of large-gap magnetic suspension systems, so that future systems can be designed with higher confidence levels.

2.0 HARDWARE DESCRIPTION

The general configuration [2] is illustrated in Figures 1,2. An array of five, room temperature, copper electromagnets are equally spaced on a 13.77 cm radius. The coils are wound with 509 turns of AWG 10 enamelled copper wire on bakelite forms, with mild steel cores. The electromagnets are mounted on an aluminum plate 1.27 cm thick. Each electromagnet is driven by a transistor switching power amplifier, rated at ± 150 V and ± 30 A continuous, with four-quadrant operation.

The suspended element consists of 16 wafers of Neodymium-Iron-Boron permanent magnet material, each 0.851 cm in diameter and 0.3175 cm thick, epoxied into an aluminum tube, 5.32 cm long and 0.9525 cm outside diameter. The total mass of the suspended element is 22.5 grams and the moment of inertia about transverse axes is 5.5×10^{-6} kg.m². The direction of magnetization is along the axis of the cylinder, which is horizontal when suspended. The nominal magnetization is 954,930 A/m (1.2 Tesla), although measurements have indicated a slightly lower working value. The suspension height is 0.1m, measured from the axis of the suspended element to the top plane of the electromagnet conductor.

The position sensing system consists of multiple light beams, arranged in the vertical and horizontal planes, partially interrupted by the suspended element. The light sources are miniature infra-red light-emitting diodes, intended for use with fiber-optics, with collimating lenses added. The light receivers are matching infra-red phototransistors, with focusing lenses added. The complete sensor system is mounted on a framework which can be rotated by hand about a vertical axis. A schematic diagram of the sensor assembly is shown in Figure 3.

Several different control systems have been developed and demonstrated, including a simple analog version with phase-advance ("lead") compensation [2], a first-generation digital controller, generated using the bilinear (Tustin's) transformation [3,4], a decoupled PD controller [5], and LQR and LQG designs [4].

3.0 MODELLING OF EDDY CURRENT EFFECTS IN LAMSTF

3.1 Introduction

Whenever a time-varying magnetic flux penetrates a conducting medium, eddy-currents will be generated. In the case of LAMSTF, the principal time variation is due to the necessary control forces and torques being generated by fluctuating electromagnet currents, since the system is open-loop unstable. In the original design, eddy-current circuits were deliberately introduced in three main areas, as illustrated in Figure 4 :

- 1) Position sensor structure, 2) Electromagnet cores, 3) Aluminum baseplate

This was done so that it would be necessary to measure, analyze and model the eddy current effects, rather than attempting to avoid their influence, as is the usual practice. The fact that stable suspension was initially achieved rather easily [2] was taken to indicate that the eddy current effects were not very significant. However, a consistent discrepancy was discovered in the dynamic behaviour in the "pitch" degree-of-freedom, illustrated in Figure 5 [3,4]. In consequence, an analysis and modelling effort was undertaken.

3.2 Simplified Eddy Current Modelling

A simplified analysis can be employed to assess the effects of eddy currents in LAMSTF. Two important initial assumptions are made:

- i) Some a priori knowledge of the geometry of the eddy current circuit
- ii) The circuit geometry is independent of frequency

The first assumption might require that the eddy currents be constrained to flow around well-defined paths, such as the position sensor structure, rather than through large plates or shells of conducting material. Alternatively, the circuit geometry must be relatively simple and predictable. The second assumption requires that the "skin depth" be much greater than the local material thickness. The skin depth is given by the following formula [6,7 etc.] :

$$\delta = \sqrt{\left(\frac{2}{\mu_0 \mu_r \sigma \omega} \right)} \quad \text{or} \quad \sqrt{\left(\frac{2\rho}{\mu_0 \mu_r \omega} \right)} \quad - (1)$$

- where $\delta =$ Skin depth (m), $\mu =$ Permeability (Hm^{-1}), $\rho = 1/\sigma =$ Resistivity (Ω), $\omega =$ angular frequency (s^{-1}). In the case of LAMSTF, the natural frequencies of the suspended element are rather low, of the order of 10Hz or less. For an aluminum conductor, the value at 10Hz would be around 28mm, much greater than the typical material thickness in LAMSTF. The only exceptions are the iron electromagnet cores, which will be discussed at some length later.

If both of the above assumptions are satisfied, the resulting model corresponds to that occasionally described in literature as the Single Time Constant Model. The derivation resembles the analysis of a transformer with a shorted secondary, as illustrated in Figure 6 :

$$V = IR + L \frac{di}{dt} + L_{m_1} \frac{di_{e_1}}{dt} + L_{m_2} \frac{di_{e_2}}{dt} + \dots \quad - (2)$$

$$0 = I_{e_n} R_{e_n} + L_{e_n} \frac{di_{e_n}}{dt} + L_{m_n} \frac{di}{dt} \quad - (3)$$

- where R_{e_n} , L_{e_n} are the resistance and inductance of the n'th eddy current circuit and L_{m_n} is the mutual inductance between the primary (the electromagnet coil) and the eddy current circuit. Note that mutual inductances between multiple eddy current circuits are neglected. The terminal characteristics of the primary (driven coil) can be found by combining these two equations :

$$\frac{I}{V} = \left(\frac{1}{(R + Ls) - \frac{(L_{m_1}s)^2}{R_{e_1} + L_{e_1}s} - \dots} \right) \quad - (4)$$

One special case is of interest here. Suppose that :

$$L = \alpha L_{e_1} \quad (0 \leq \alpha \leq \infty) \quad \text{and} \quad L_{m_1} = \beta \sqrt{L L_{e_1}} \quad (0 \leq \beta \leq 1) \quad - (5)$$

then :

$$\frac{I}{V} = \left(\frac{1}{(R + Ls) - \frac{\beta^2 \alpha (L_{e_1}s)^2}{R_{e_1} + L_{e_1}s} - \dots} \right) \quad - (6a)$$

but if $R_{e_1} \rightarrow 0$ or $s \rightarrow \infty$:

$$\frac{I}{V} = \left(\frac{1}{R + Ls(1-\beta^2)} \right) \quad - (6b)$$

This confirms that a non-dissipative (reactive) secondary effectively “turns off” part of the primary inductor. Continuing, the field components generated (at the suspended object) can be expressed as :

$$B_j = K_j I + K_{e_j} I_{e_1} + \dots = K_j I \left(1 - \frac{K_{e_j} L_{m_1} s}{K_j (R_{e_1} + L_{e_1} s)} - \dots \right) \quad - (7)$$

- where K_j , K_{e_n} are constants representing the j'th field component generated at the suspension location by the electromagnet and the n'th eddy current respectively. Now the factor K_{e_n} will, in general, be different for each field component, that is each individual eddy current will affect each field component by a different proportion, compared to the main electromagnet. Therefore the eddy current effects in a system involving several electromagnets and eddy current circuits should be represented as follows :

$$[B_j] = [K_j] [I] + [K_{j_e}] [I_e] \quad - (8)$$

- where $[B_j] = (B_x \ B_y \ B_z \ B_{xx} \ \dots)^T$, $[I] = (I_1 \ I_2 \ \dots)^T$, $[K_j]$ is a rectangular matrix of field coefficients and $[K_{j_e}]$ is similar, though possibly of differing dimension. It is presumed that $[I_e]$ can be derived from $[I]$, following equations 2,3.

Alternatively, if the eddy current circuit has similar geometry to the primary (for example the induced current in electromagnet cores), it can be argued that the relative effect on all field and field gradient components at the suspended object will be similar. In this case, the representation can be considerably simplified by invoking a false current as shown :

$$I' = \left(1 - \frac{K_{e_1} L_{m_1} s}{K_j (R_{e_1} + L_{e_1} s)} - \dots \right) I, \quad \text{where } B_j = K_j I' \quad - (9)$$

It should be noted that the change in electromagnet terminal characteristics and the change in field at the model are two separate effects and should be modelled as such.

3.3 Alternative Representations - The Circuit Model

The preceding analysis was cast in simple terms, based on the concept of flux linkages between electrically separate circuits. This corresponds to the physical situation, and is a reasonably comprehensible representation for non-specialists. A significant amount of previous literature does exist in the area of eddy current modelling, but is mostly cast in terms more familiar to electrical engineers, namely circuit impedances [8,9,10 etc.]. So as to clarify the equivalences between different approaches, an alternative representation will now be established.

Considering a single coil, wound on a dissipative core, illustrated in Figure 7, the equation governing the magnetic excitation is as follows :

$$\text{MMF} = G_e \frac{d\phi}{dt} + \frac{1}{P} \phi \quad - (10)$$

- where MMF is the magnetomotive force (ampere-turns) driving the magnetic circuit, G_e is the electrical conductance (inverse of resistance) and P is the magnetic permeance. The magnetic impedance is defined as the complex ratio of MMF to flux rate :

$$Z_m = \frac{\text{MMF}}{\phi} \quad - (11)$$

Now using equation 10 and assuming sinusoidal excitation as usual :

$$Z_m = \frac{sPG_e + 1}{sP} \quad - (12)$$

Now the concept of the "gyrator" is introduced, wherein the magnetic impedance can be related to the electrical impedance of the exciting coil :

$$Z_e = \frac{N^2}{Z_m} \quad - (13)$$

The terminal characteristics of the coil can now be established :

$$\frac{1}{V} = \frac{1}{Z_T} = \frac{1}{R + Z_e} = \frac{1}{R + \frac{N^2 P_s}{1 + PG_e s}} \quad - (14)$$

This is equivalent to equation 4 above, as can be verified with the following substitutions and manipulations :

$$L_{e_1} = \frac{L}{N^2} \quad (\text{assume eddy current geometry resembles driving coil}) \quad - (15a)$$

$$L_{m_1} = \sqrt{L L_{e_1}} = \frac{L}{N} \quad (\text{perfect flux linkage to eddy current circuit}) \quad - (15b)$$

$$R_{e_1} = \frac{1}{G_{e_1}} \quad (\text{definition}) \quad - (15c)$$

$$L = N^2 P \quad (\text{definition}) \quad - (15d)$$

Note that equations 15a and 15d indicate that $P = L_{e_1}$ in this representation.

4.0 EXPERIMENTAL MEASUREMENTS

4.1 Determination of Parameters

The question now is, can the parameters K_{e_n} , L_{e_n} , R_{e_n} and L_{m_n} be estimated and/or measured with sufficient accuracy? First the problem of estimation is addressed.

Calculations have been carried out using the finite element computer code VF/GFUN, by Vector Fields Inc.. It should be noted that this code is magnetostatic and has no capability for direct eddy current calculations, although such codes are available (for instance ELEKTRA,

by the same supplier). Instead, the code is used to calculate flux linkages, hence inductances, using :

$$\phi_{ij} = \frac{\phi_i}{I_j} = \frac{\int_i \int_j B \cdot ds}{I_j} \quad - (16)$$

VF/GFUN calculates the field on a grid representing the linkage plane of the eddy current circuit. The field normal to the plane is then numerically integrated (by the OPERA pre- and post-processor) to yield the flux linkage term. Figure 8 illustrates the general arrangement. The calculation of the $K_{e_{in}}$ terms is straightforward.

By way of example, a series of calculations has been made for a single LAMSTF electromagnet with a representation of one part of the position sensor assembly mounted on the same axis, as illustrated in Figure 9. The required parameters were predicted (or previously measured) to be :

$$\begin{array}{ll} L = 0.0275 \text{ H} & R = 0.74 \Omega \\ L_e = 6.69 \times 10^{-7} \text{ H} & R_e = 2.243 \times 10^{-4} \Omega \\ L_m = 1.0998 \times 10^{-5} \text{ H} & \\ K_z = 3.495 \times 10^{-4} \text{ T} & K_{z_e} = 4.369 \times 10^{-6} \text{ T} \end{array}$$

Incorporating these values in equation 7, and examining the axial (z-axis) field component, gives :

$$B_z = K_z I \left(1 - \frac{6.13 \times 10^{-4} \text{ s}}{1 + 2.983 \times 10^{-3} \text{ s}} \right) \quad - (17)$$

It is seen that the resonant frequency of this eddy current circuit is around 53Hz, significantly higher than LAMSTF open-loop natural frequencies, but still well within the range of interest.

4.2 Experimental Verification

Actual measurements of the current to field transfer function, corresponding to equation 7, were made with an experimental set-up as described above, and later with LAMSTF. Field components were measured with a F.W. Bell Model 9903 Hall-effect gaussmeter. Electromagnet currents were measured using a current shunt. The transfer function was measured directly with a Schlumberger Model SI 1250 analyzer, with sine-sweep excitation. The results for an air-cored electromagnet with no eddy current circuits are shown in Figure 10, and are taken to represent the probe + instrument + data acquisition system response. These results are subtracted from all subsequent measurements. Figure 11 shows the measured transfer function for B_z , together with the predictions from equation 17. The agreement is thought to be satisfactory. The values of most parameters can be adjusted (refined) to give a better agreement, as shown in Figure 12. The only significant residual discrepancies are seen to occur at higher frequencies where the validity of the Single Time Constant Model is questionable.

The adjusted form of equation 17 is :

$$B_z = K_z I \left(1 - \frac{7.591 \times 10^{-4} \text{ s}}{1 + 2.934 \times 10^{-3} \text{ s}} \right) \quad - (17b)$$

4.2.1 Parameter Adjustment Procedure

If equation 17 is written :

$$B_j = K_j I \left(1 - \frac{as}{1+bs} \right) \quad - (18)$$

- then it is easily shown that the maximum phase lag occurs at a frequency given by :

$$\omega_{\phi_{\max}} = \sqrt{\left(\frac{1}{b^2 - ab} \right)} \quad - (19)$$

- that the maximum phase lag is :

$$\phi_{\max} = \text{Tan}^{-1} \left(\frac{a}{2\sqrt{(b^2 - ab)}} \right) \quad - (20)$$

- and that the infinite frequency gain attenuation is :

$$\text{db}_{\omega \rightarrow \infty} = 20 \log_{10} \left(1 - \frac{a}{b} \right) \quad - (21)$$

In most cases, the maximum phase lag and the frequency for maximum phase lag are the easiest to apply, and are sufficient to specify the parameters a and b, using :

$$a = \frac{2 \text{Tan}(\phi_{\max})}{\omega_{\phi_{\max}}} \quad \text{and} \quad b = \frac{a}{2} + \sqrt{\left(\frac{a^2}{4} + \frac{1}{\omega_{\phi_{\max}}^2} \right)} \quad - (22)$$

4.3 More Complex Cases

If the electromagnet is mounted on the aluminum plate, a second eddy current circuit is added; when the iron core is inserted, a third is added. Figures 13-15 show the comparison between experimental and computed responses. Again, the agreement is fair, although capable of improvement by refinement of parameter estimates, also shown in Figures 13-15. Note that, even if refinement of parameters is undertaken, the model does not correctly predict the high frequency behaviour, particularly where the iron core is present. This is due to the iron core becoming highly dissipative at these frequencies, due to its small skin depth.

An additional series of calculations and measurements has been made for the vertical field component generated at the centroid of the suspended element due to a LAMSTF electromagnet at the design location, i.e. with the sensor ring off-axis relative to the electromagnet. The geometry is illustrated in Figure 16 and typical measured responses is shown in Figure 17. It is clear that the model is progressively less suitable for progressively more complex geometries.

Measurements have also been made with the full LAMSTF sensor frame in place. Examples are shown in Figure 18. Due to the geometrical complexity, with multiple interlocking eddy current paths, it has not yet been possible to compute reasonable estimates by the methods shown. It should be noted, however, that another assumption inherent in the form of the model previously chosen has been violated, that is the lack of interaction between separate eddy circuits. If these circuits are physically and electrically connected, this is clearly not reasonable.

4.4 Terminal Characteristics

It appears to be possible to experimentally estimate certain important parameters without direct measurement of magnetic fields. Figure 19 shows a comparison of measured and computed terminal characteristics for the single LAMSTF electromagnet mentioned above. The agreement is not perfect, but sufficient to validate the approach and can, of course, be improved by adjustment of parameters.

5.0 ADVANCED EDDY CURRENT MODELLING

5.1 Introduction

The discrepancies between the modelled and measured responses with the iron core present are confined to the higher frequencies. They are manifested as reduced intensity and increased phase lag of the magnetic field, compared to the simple model described above. The simple analytic model cannot be adjusted or manipulated so as to satisfactorily model this behaviour. However, by studying some more simplified geometries, where analytic solutions are available, insight into the correct form of a more elaborate and realistic model can be gained. The cases to be studied are the magnetization of an infinite sheet by an in-plane uniform applied field and the magnetization of an infinite cylindrical bar by a uniform axial field.

5.2 Magnetization of an Infinite Flat Sheet

This is a classical problem, whose solution can be found in numerous texts [6,7,11,12] and which is illustrated in Figure 20. The outline is shown here for reference. The governing equation is the 1-dimensional diffusion equation :

$$\frac{\partial^2 B_z}{\partial y^2} = \sigma \mu_o \mu_r \frac{\partial B_z}{\partial t} \quad - (23)$$

This can also be written in terms of H_z , or, in an alternative form, in terms of J_x . The general solution to this equation is :

$$B_z = K_1 e^{\alpha y} + K_2 e^{-\alpha y} \quad - (24)$$

$$\text{where } \alpha = \sqrt{j\omega\sigma\mu_o\mu_r} = \frac{1+j}{\delta} \text{ as } \delta = \sqrt{\left(\frac{2}{\omega\sigma\mu_o\mu_r}\right)} \quad - (25)$$

From the boundary conditions of $B = B_s$ @ $y = \pm b$, we find :

$$K_1 = K_2 = \frac{B_s}{e^{\alpha b} + e^{-\alpha b}} \quad - (26)$$

So that :

$$B = B_s \left(\frac{\text{Cosh}(\alpha y)}{\text{Cosh}(\alpha b)} \right) \quad - (27)$$

This is plotted as Figure 21. Integrating the total flux across the conductor :

$$B_{\text{total}} = \frac{2B_s \text{Sinh}(\alpha b)}{\alpha \text{Cosh}(\alpha b)} \quad - (28)$$

Now expanding the hyperbolic functions as infinite series :

$$B_{\text{total}} = 2B_s b \left(\frac{1 + \frac{(\alpha b)^2}{3!} + \frac{(\alpha b)^4}{5!} + \frac{(\alpha b)^6}{7!} + \dots}{1 + \frac{(\alpha b)^2}{2!} + \frac{(\alpha b)^4}{4!} + \frac{(\alpha b)^6}{6!} + \dots} \right) \quad - (29)$$

Where :

$$(\alpha b)^2 = j\omega (\sigma \mu_o \mu_r b^2) \quad - (30)$$

It is recognized that equation 29 represents a pole-zero sequence, with a d.c. response of $2B_s b$. The obvious approach to modelling is to approximate using the first few terms of the series. Figure 22 shows the response for various numbers of terms. It is seen that large fluctuations in response occur at higher frequencies with larger numbers of terms. This is due to the generation of lightly damped, closely spaced poles, coupled with series truncation error. In practice, only a few terms would be employed in any case, to avoid excessive complexity in the model. By inspection, a four- or five-term series seems to be a reasonable choice.

It should also be noted that the limiting rate of roll-off (i.e. at high frequencies) is 10db/decade and that the limiting phase lag is 45° . Both of these values is exactly half the corresponding value for a simple first-order pole.

5.3 Magnetization of an Infinite Cylindrical Bar

The magnetization of an infinitely long cylindrical bar in a uniform, axially applied field is again a classical problem whose solution can be found in a number of texts [6,7 etc.]. The geometry is shown in Figure 23. The governing equation is the diffusion equation :

$$\nabla^2 B = \sigma \mu_o \mu_r \frac{\partial B}{\partial t} \quad - (31)$$

In cylindrical coordinates, for an axisymmetric problem, this reduces to :

$$\frac{\partial^2 B_x}{\partial r^2} + \frac{1}{r} \frac{\partial B_x}{\partial r} = \sigma \mu_o \mu_r \frac{\partial B_x}{\partial t} \quad - (32)$$

For the case of sinusoidal excitation, we assume $B_x = B(r) e^{j\omega t}$ and the spatial part of the problem reduces to the form of Bessel's equation :

$$\frac{d^2 B_x}{dr^2} + \frac{1}{r} \frac{dB_x}{dr} - j\omega\sigma\mu_o\mu_r B_x = 0 \quad - (33)$$

The solution of this equation is of the form :

$$B = A_1 J_0(\alpha r) + A_2 J_{-0}(\alpha r) \quad - (34)$$

- where J_0 and J_{-0} are zero-order Bessel functions of the first and second kind respectively, and α has the same definition as previously. Since a finite field is required on the axis ($r = 0$), the coefficient A_2 must be 0. With the boundary condition of $B = B_s$ at $r = a$, the solution becomes :

$$B = B_s \frac{J_0(j\alpha r)}{J_0(j\alpha a)} \quad - (35)$$

- which can be expressed as an infinite series :

$$B = B_s \frac{1 + \frac{(\alpha r/2)^2}{1!^2} + \frac{(\alpha r/2)^4}{2!^2} + \frac{(\alpha r/2)^6}{3!^2}}{1 + \frac{(\alpha a/2)^2}{1!^2} + \frac{(\alpha a/2)^4}{2!^2} + \dots} \quad - (36)$$

This is plotted in Figure 24. Again integrating the total flux across the conductor :

$$B = \pi B_s a^2 \frac{1 + \frac{(\alpha a/2)^2}{2 \cdot 1!^2} + \frac{(\alpha a/2)^4}{3 \cdot 2!^2} + \frac{(\alpha a/2)^6}{4 \cdot 3!^2}}{1 + \frac{(\alpha a/2)^2}{1!^2} + \frac{(\alpha a/2)^4}{2!^2} + \dots} \quad - (37)$$

This is shown in Figure 25.

6.0 SCALING of EDDY CURRENTS

Whenever sub-scale tests are contemplated, it is necessary to understand how the phenomena under investigation scales with linear dimension. For instance, in this case, sub-scale tests may well be required to validate predicted eddy current models, or even to provide design values for some parameters.

For the case of conducting ring of given geometry and scale S , as shown in Figure 26, it is immediately apparent that :

$$R \propto \rho \frac{S}{A} \propto \frac{\rho}{S} \quad L \propto N^2 S \quad \text{Therefore } - \frac{L}{R} \propto S^2 \quad - (38)$$

Of course the proposed dynamic models (for instance see equation 4) are composed of terms of the form $(R + j\omega L)$. Now recalling the skin depth formula :

$$\delta = \sqrt{\left(\frac{2}{\mu_0 \mu_r \sigma \omega}\right)} \propto \frac{1}{\sqrt{\omega}} \quad - (39)$$

In either case it is clear that dynamic similarity can be achieved if the excitation frequencies are scaled as follows :

$$\omega \propto \frac{1}{S^2} \quad - (40)$$

7.0 DISCUSSION

The eddy current models proposed appear to be satisfactory in the case of large eddy current circuits in conducting, magnetic, or non-magnetic material. Relatively simple computations are capable of providing reasonable estimates of important parameters, with the option of refinement based on measurements of magnetic field or electromagnet terminal characteristics. The most difficult case is seen to be that of eddy currents in magnetic material, due to the lower skin depths. However, discrepancies at frequencies well outside (above) the controller bandwidth would be of no particular consequence in this case.

The simple models are not adequate to fully describe the eddy currents in the LAMSTF position sensor structure, due to its geometric complexity. This leads to difficulties in parameter estimation and strong coupling between multiple eddy current circuits.

8.0 CONCLUSIONS

Simple models for the effect of eddy currents in the metallic structure of LAMSTF has been proposed and validated by experiment. However, it has not yet been possible to fully describe the eddy currents in the position sensor framework due to the geometric complexity involved.

Eddy currents have been shown to seriously affect field and field gradient components in the frequency range of interest, such that they must be incorporated into a system dynamic model if modern control synthesis techniques are to be fully successful.

ACKNOWLEDGEMENTS

This work was supported by NASA Langley Research Center under Grant NAG-1-1056. The Technical Monitor was Nelson J. Groom of the Guidance and Control Branch.

REFERENCES

1. Britcher, C.P.: Large-Gap Magnetic Suspension Systems. International Symposium on Magnetic Suspension Technology. NASA Langley Research Center, August 1991. NASA CP-3152 .
2. Britcher, C.P.; Ghofrani, M.; Britton, T.; Groom, N.J.: The Large-Angle Magnetic Suspension Test Fixture. International Symposium on Magnetic Suspension Technology. NASA Langley Research Center, August 1991. NASA CP-3152 .
3. M. Ghofrani, Approaches to Control of the Large-Angle Magnetic Suspension Test Fixture. NASA CR-191890, December 1992. ✓
4. Groom, N.J.; Britcher, C.P.: A Description of a Laboratory Model Magnetic Suspension Test Fixture with a Large Angular Capability. 1st IEEE Conference on Control Applications, Wright-Patterson AFB, September 1992.
5. Cox, D.; Groom, N.J.: A Decoupled Control Approach for a Large-Gap Magnetic Suspension System. 2nd International Symposium on Magnetic Suspension Technology, Seattle, WA, August 1993.
6. Stoll, R.L.: The Analysis of Eddy Currents. Clarendon, 1974
7. Binns, K.J.; Lawrenson, P.J.; Trowbridge, C.W.: The Analysis and Computation of Electric and Magnetic Fields. Wiley, 1992.
8. Buntenbach, R.W.: Improved Circuit Models for Inductors Wound on Dissipative Magnetic Cores. 2nd Asilomar Conference on Corcuits and Systems, 1968.
9. Cherry, E. C.:The Duality between Interlinked Electric and Magnetic Circuits and the Formulation of Transformer Equivalent Curcuits. Proceedings of the Physical Society of London, February 1949.
10. Downer, J.R.: Analysis of a Single-Axis Magnetic Suspension System. MIT Master's thesis, January 1980.
11. Moon, P.; Spencer, D.E.: Field Theory for Engineers. Van Nostrand, various.
12. Wylie, C.R. Jnr.: Advancted Engineering Mathematics. McGraw-Hill, various.

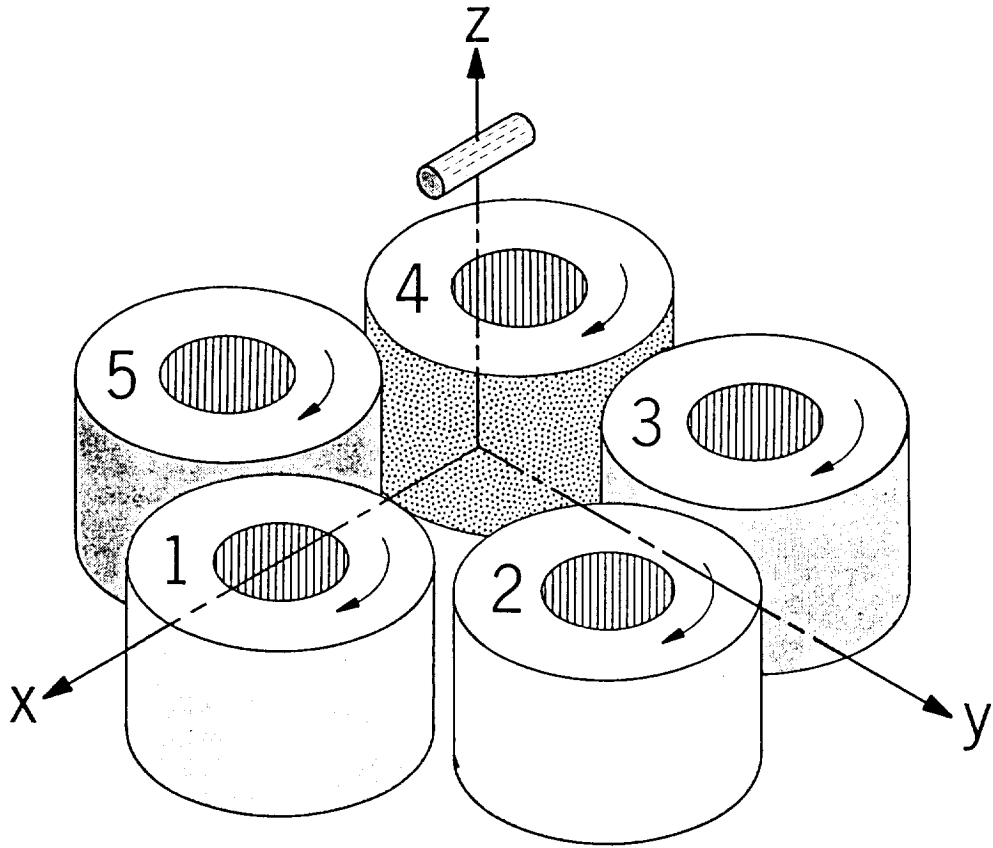


Figure 1 - General Arrangement of the Large Angle Magnetic Suspension Test Fixture

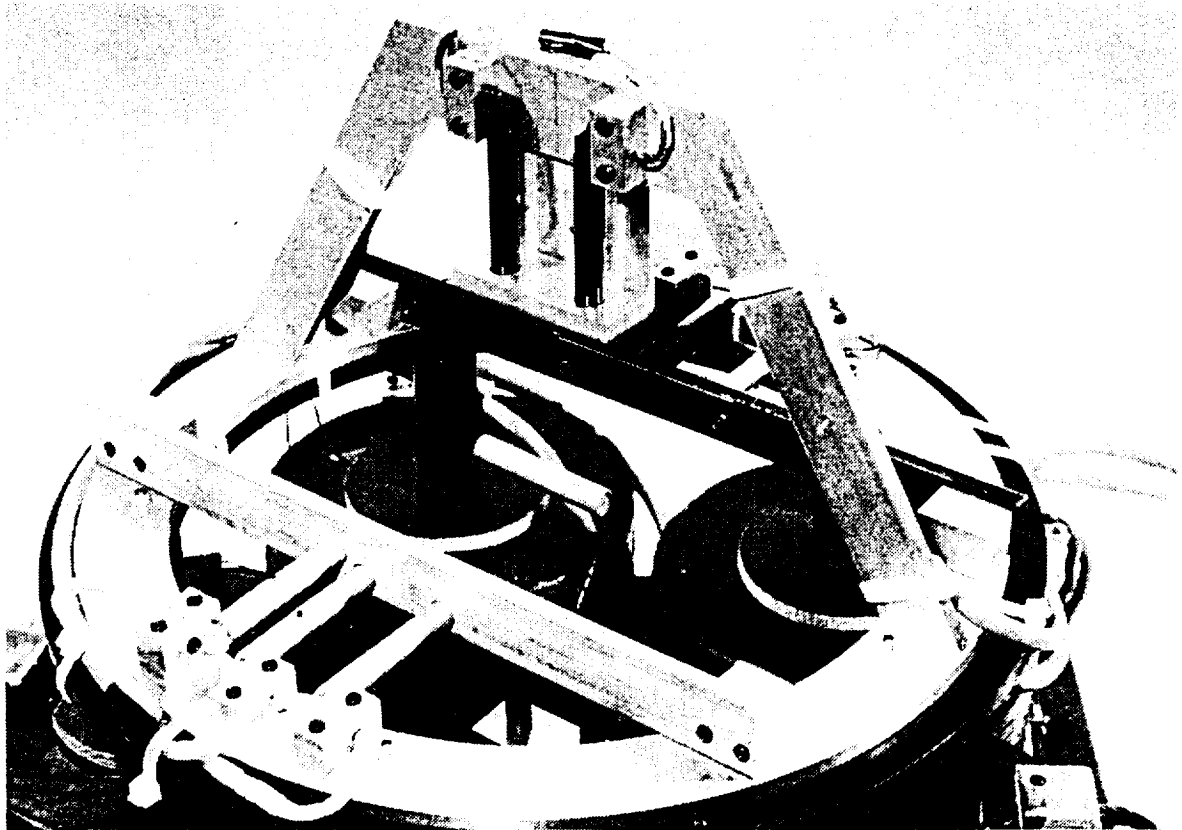


Figure 2 - The Large Angle Magnetic Suspension Test Fixture

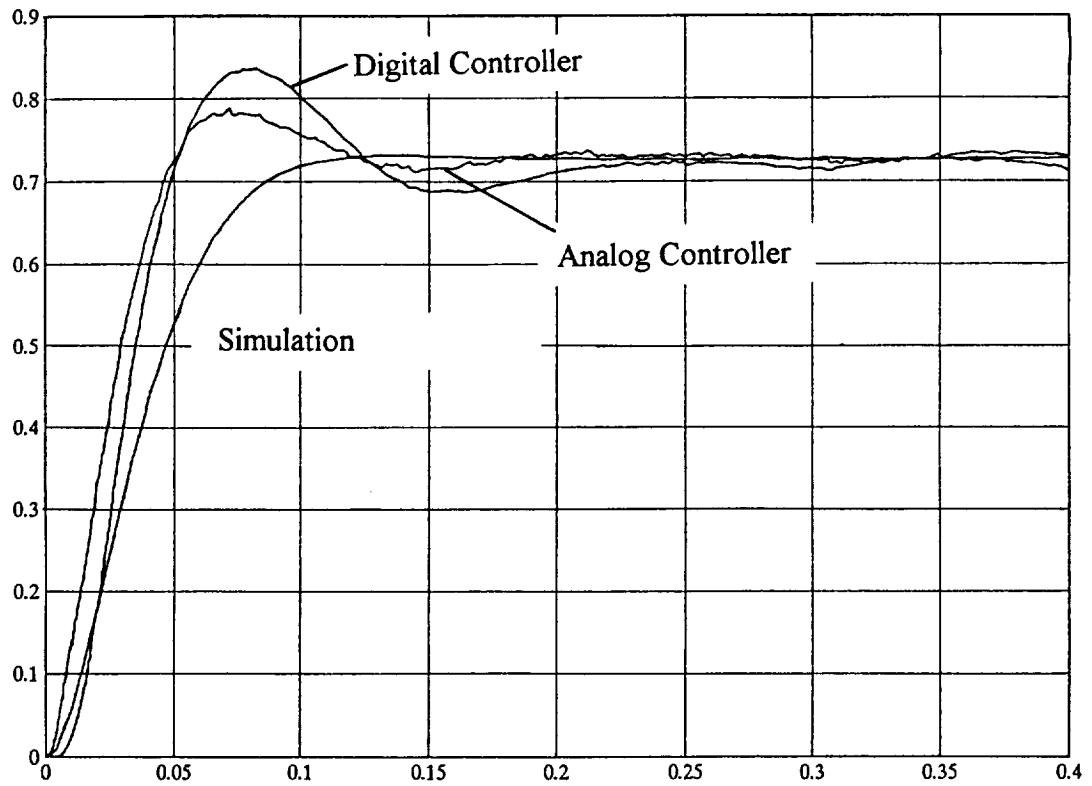


Figure 5 - Initial Discrepancy in Dynamic Response in Pitch (θ_y)

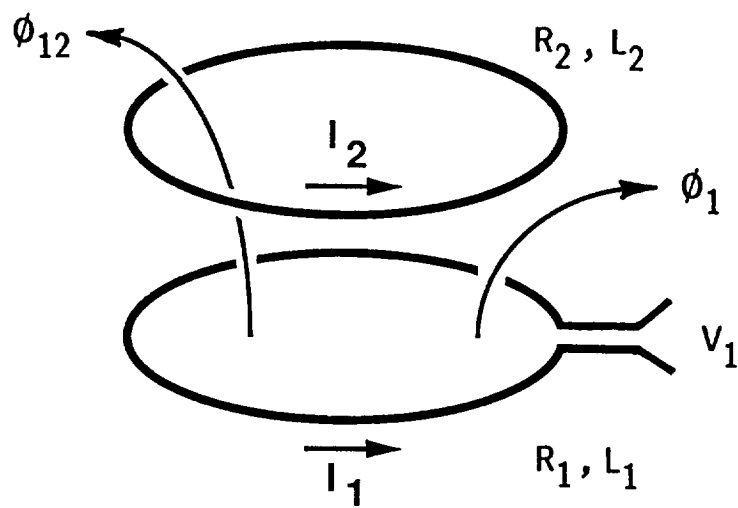


Figure 6 - Schematic of Circuit Model for Primary to Secondary Coupling

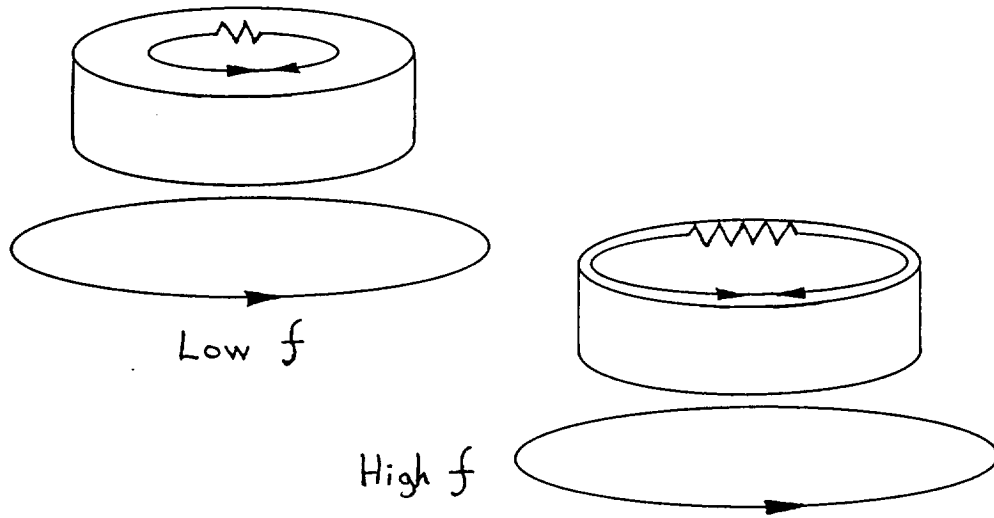


Figure 7 - Schematic Diagram of a Coil on a Dissipative Core

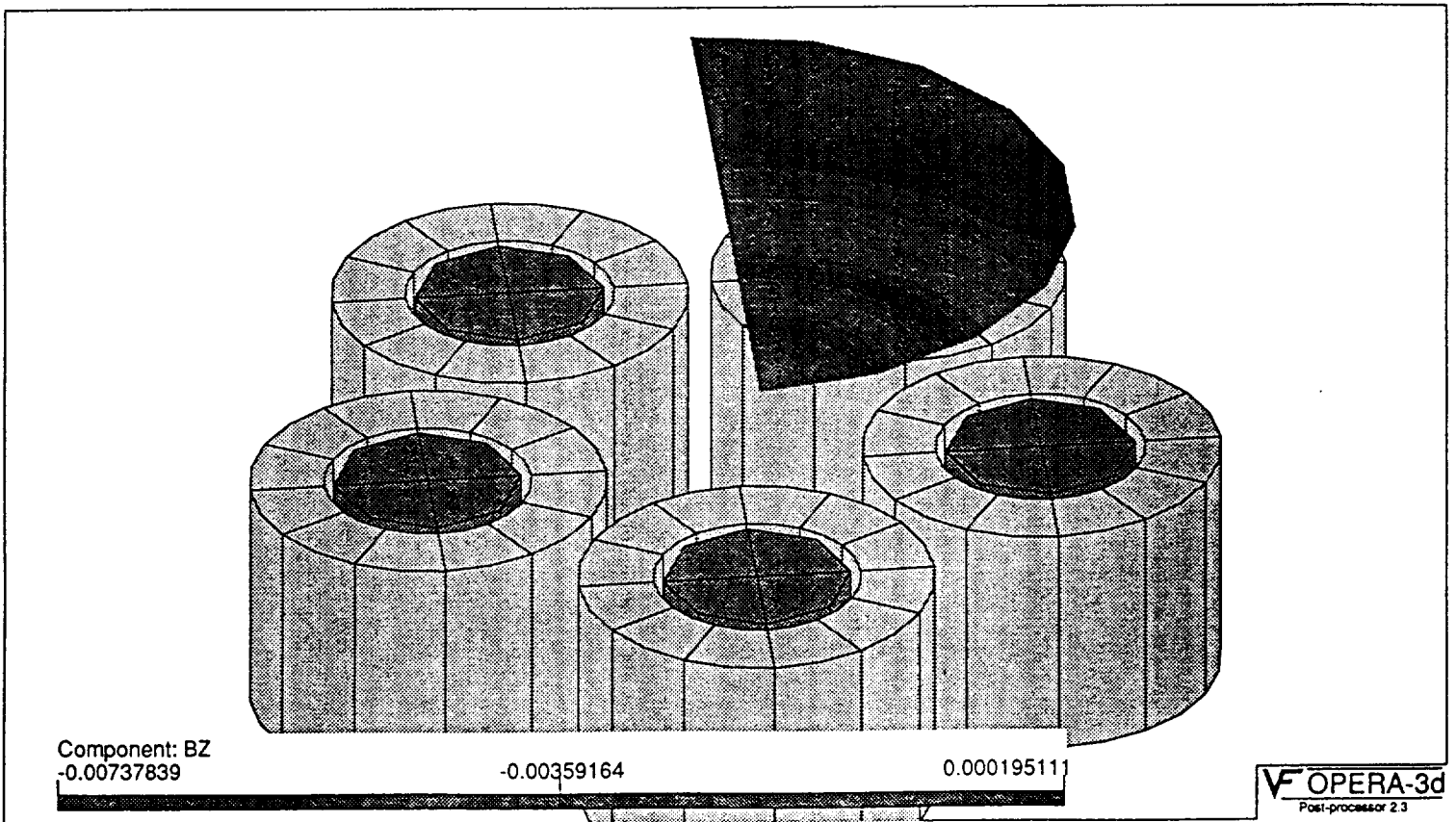


Figure 8 - Illustration of OPERA Flux Linkage Computation (B_z shown)

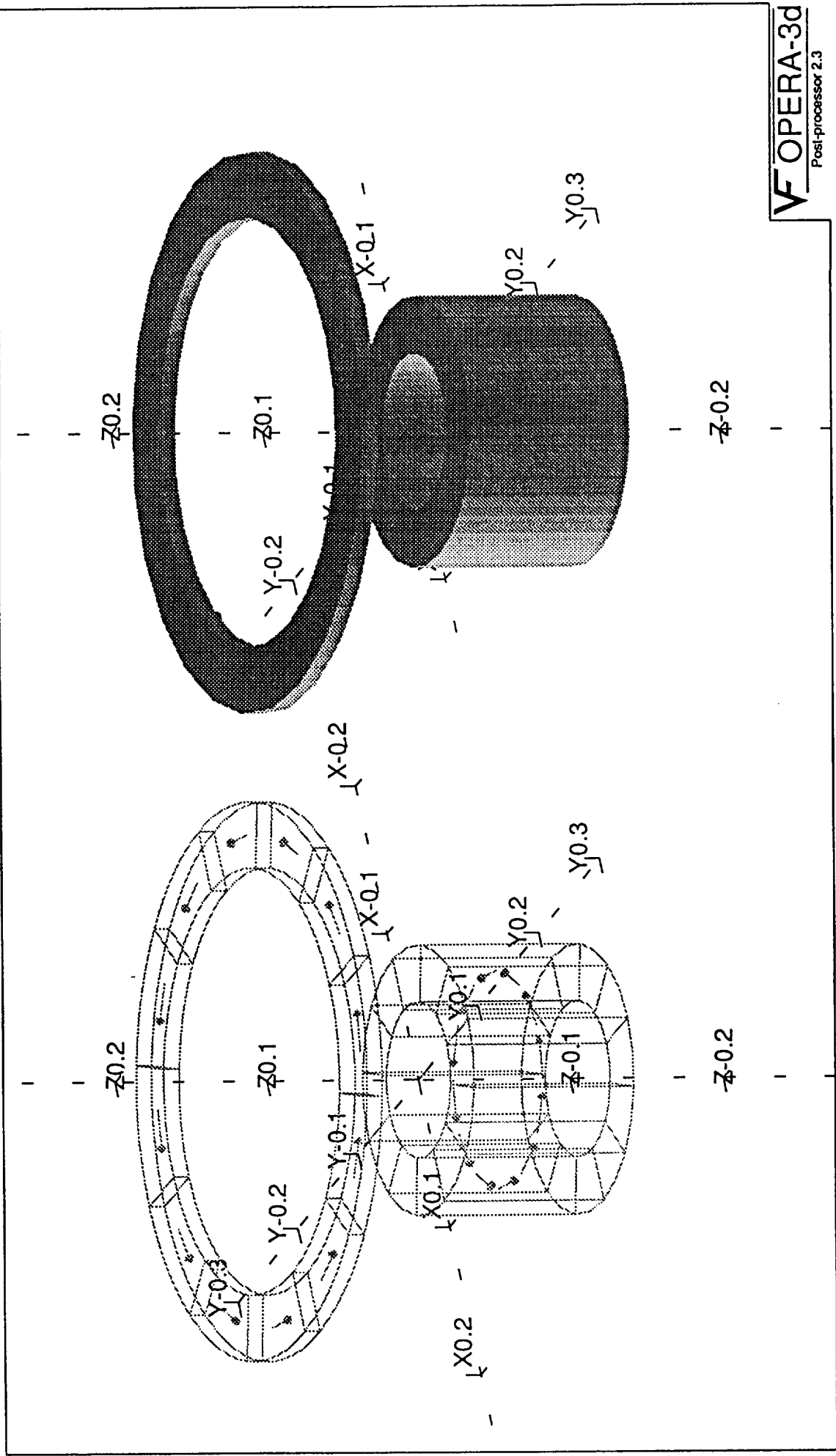


Figure 9 - Simplified Eddy Current Test Set-Up

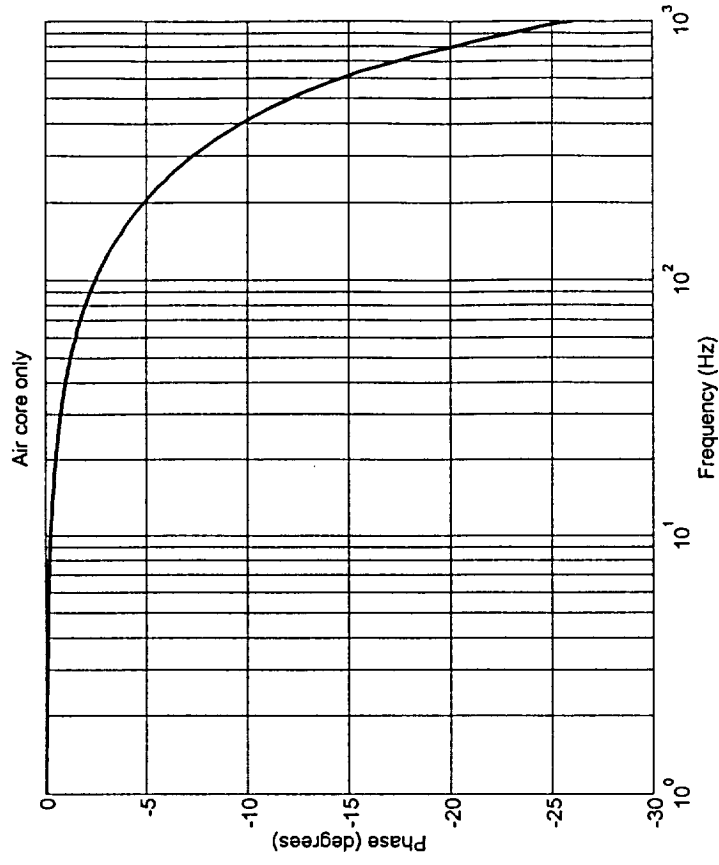
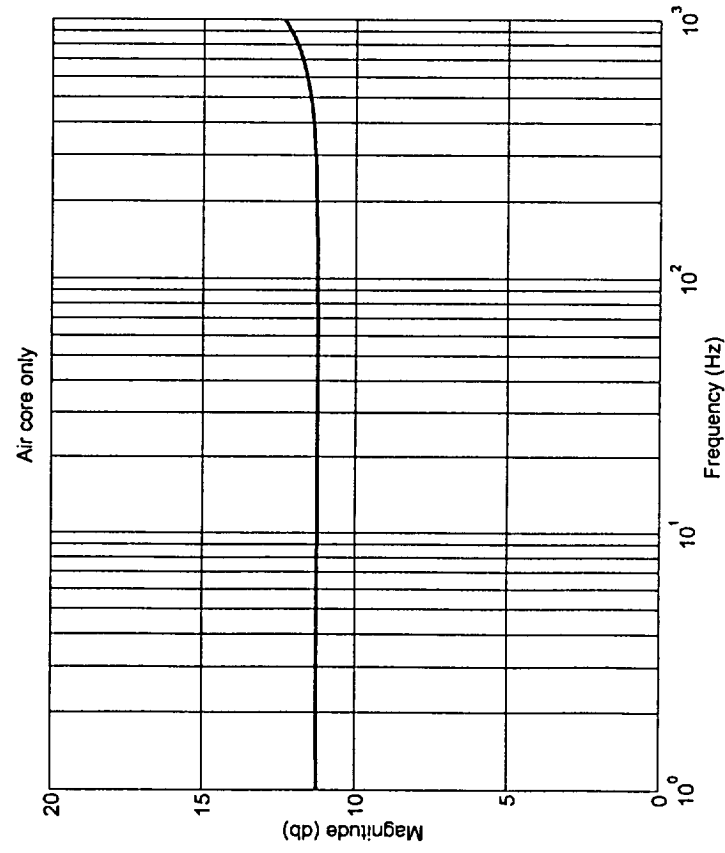


Figure 10 - Gaussmeter Probe Response

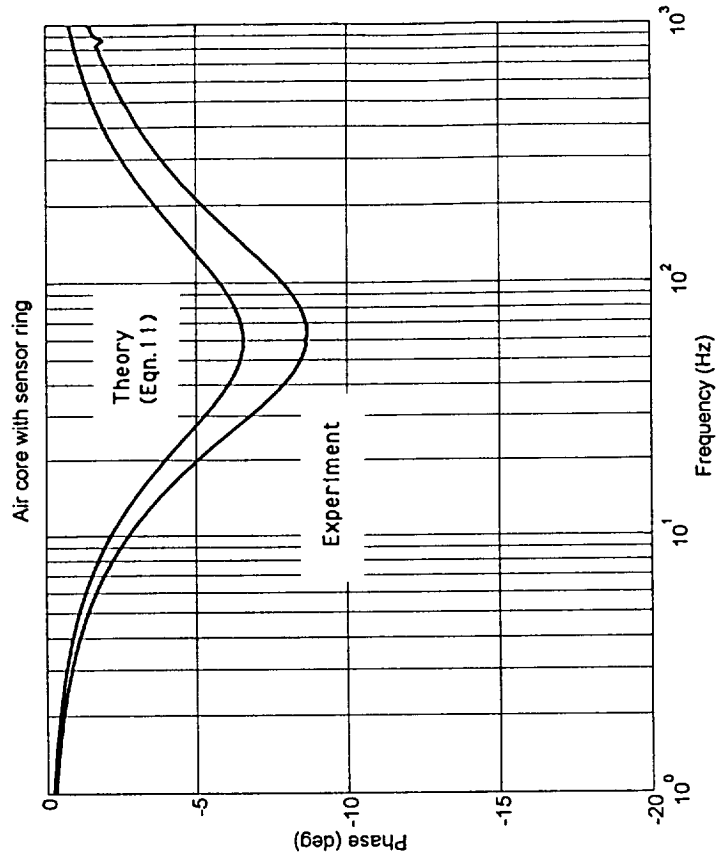
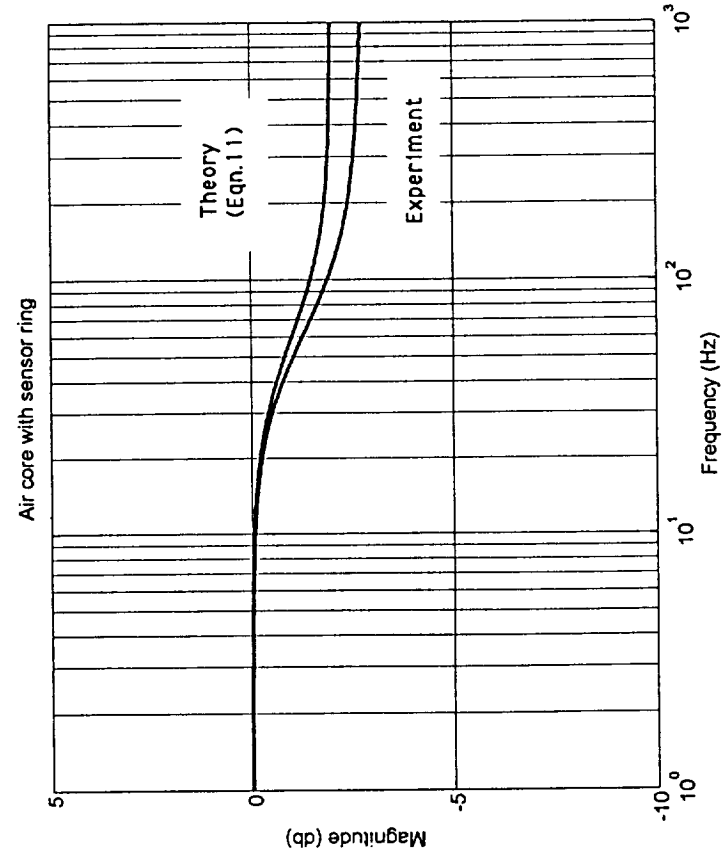


Figure 11 - Axial Field for Air-Cored Electromagnet and Dummy Sensor Ring

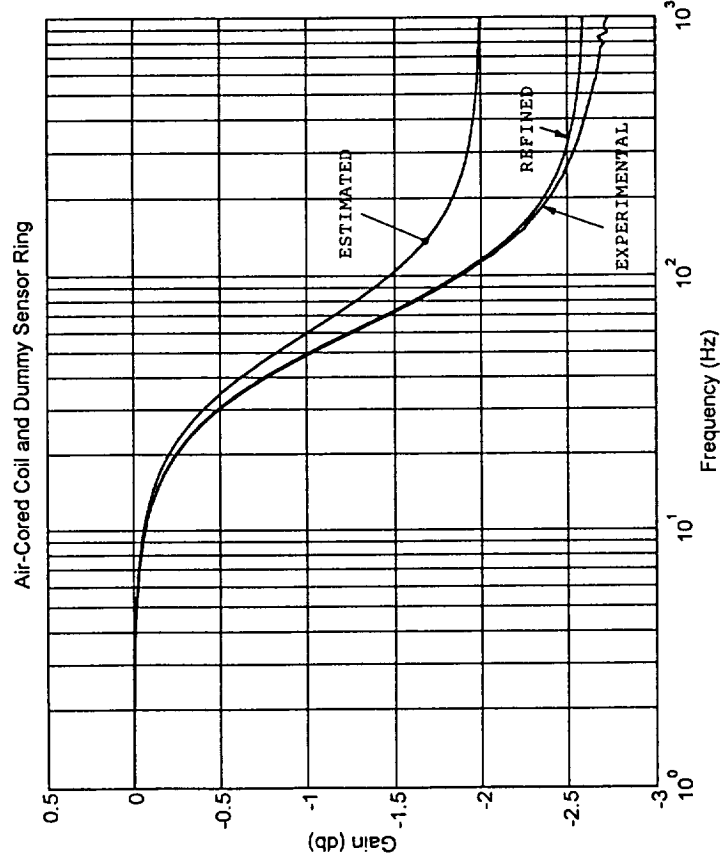
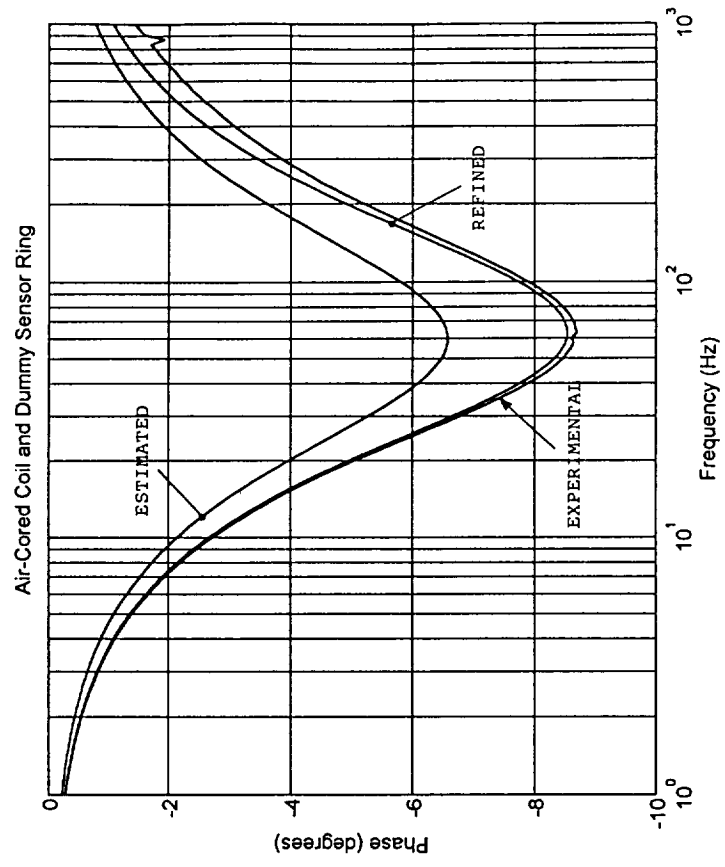


Figure 12 - Axial Field with Adjusted Parameters

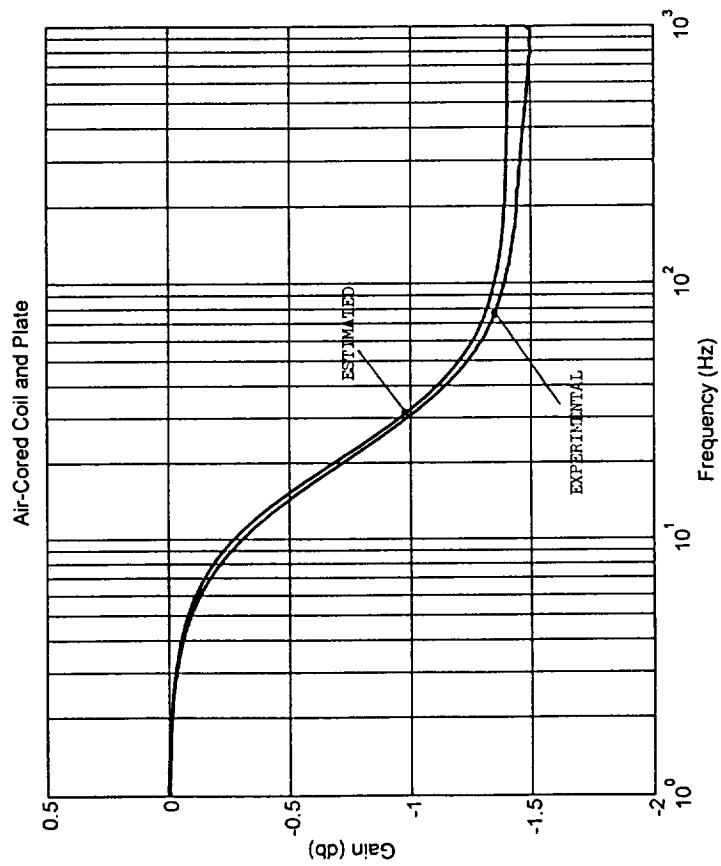
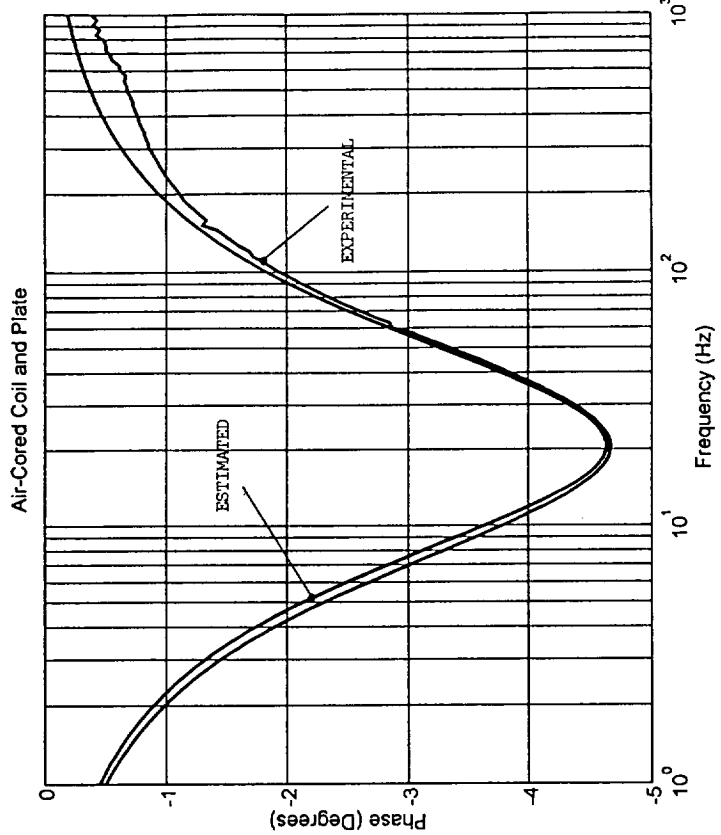


Figure 13 - Axial Field with Alloy Plate Added

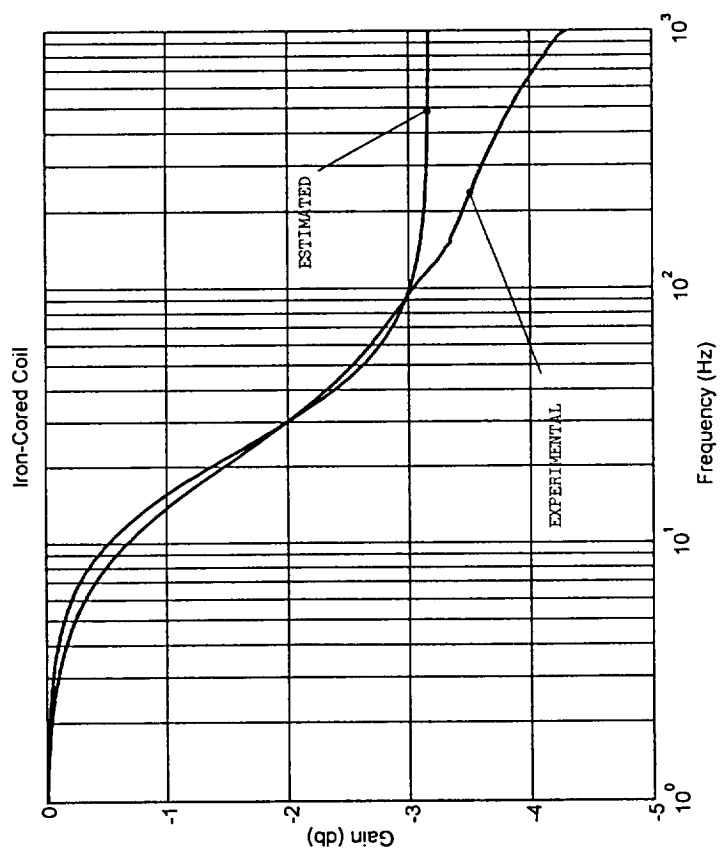
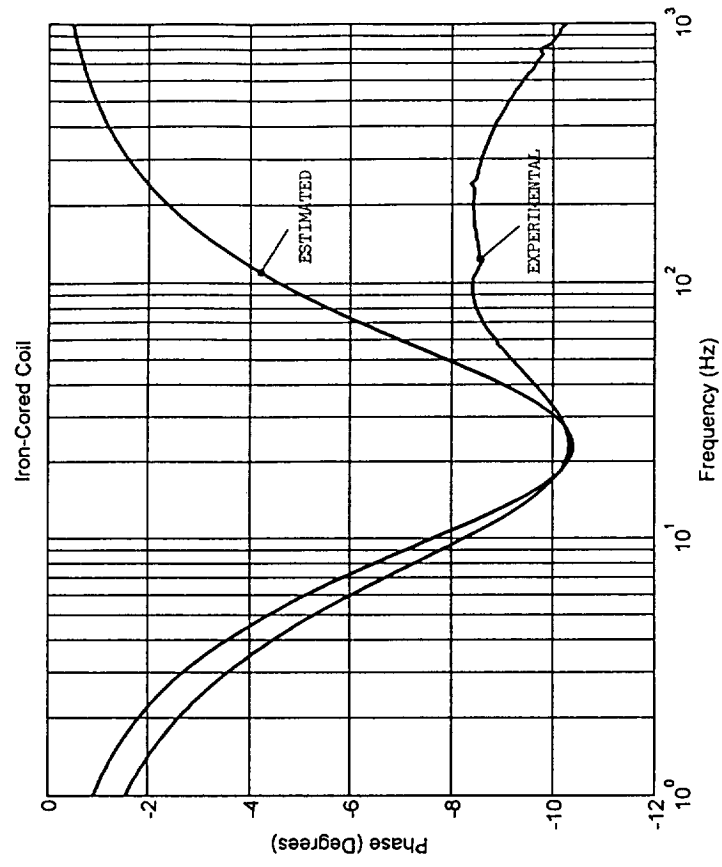


Figure 14 - Axial Field with Iron Core Added

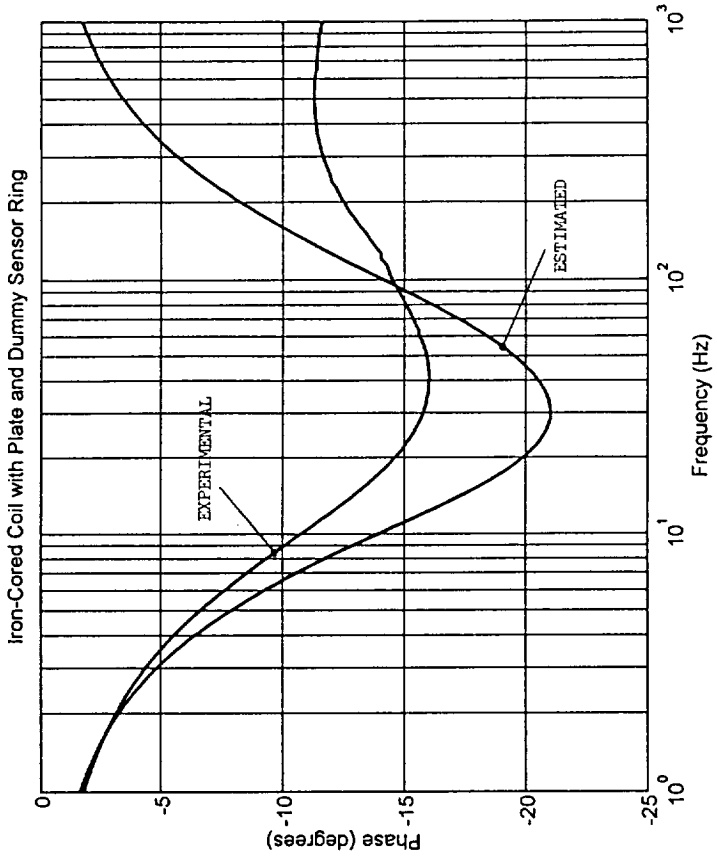
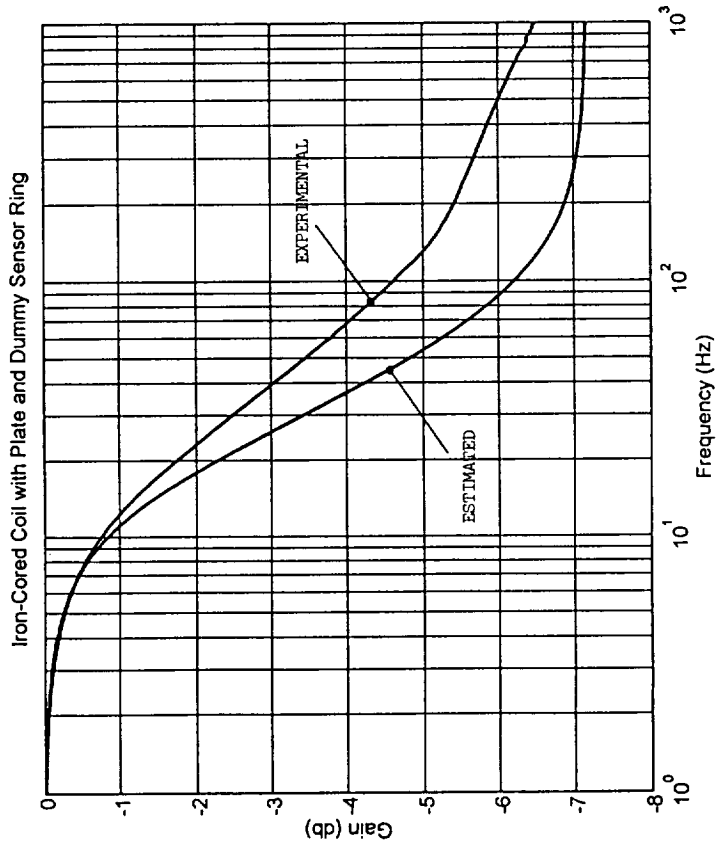


Figure 15 - Axial Field with Iron Core and Alloy Plate Added

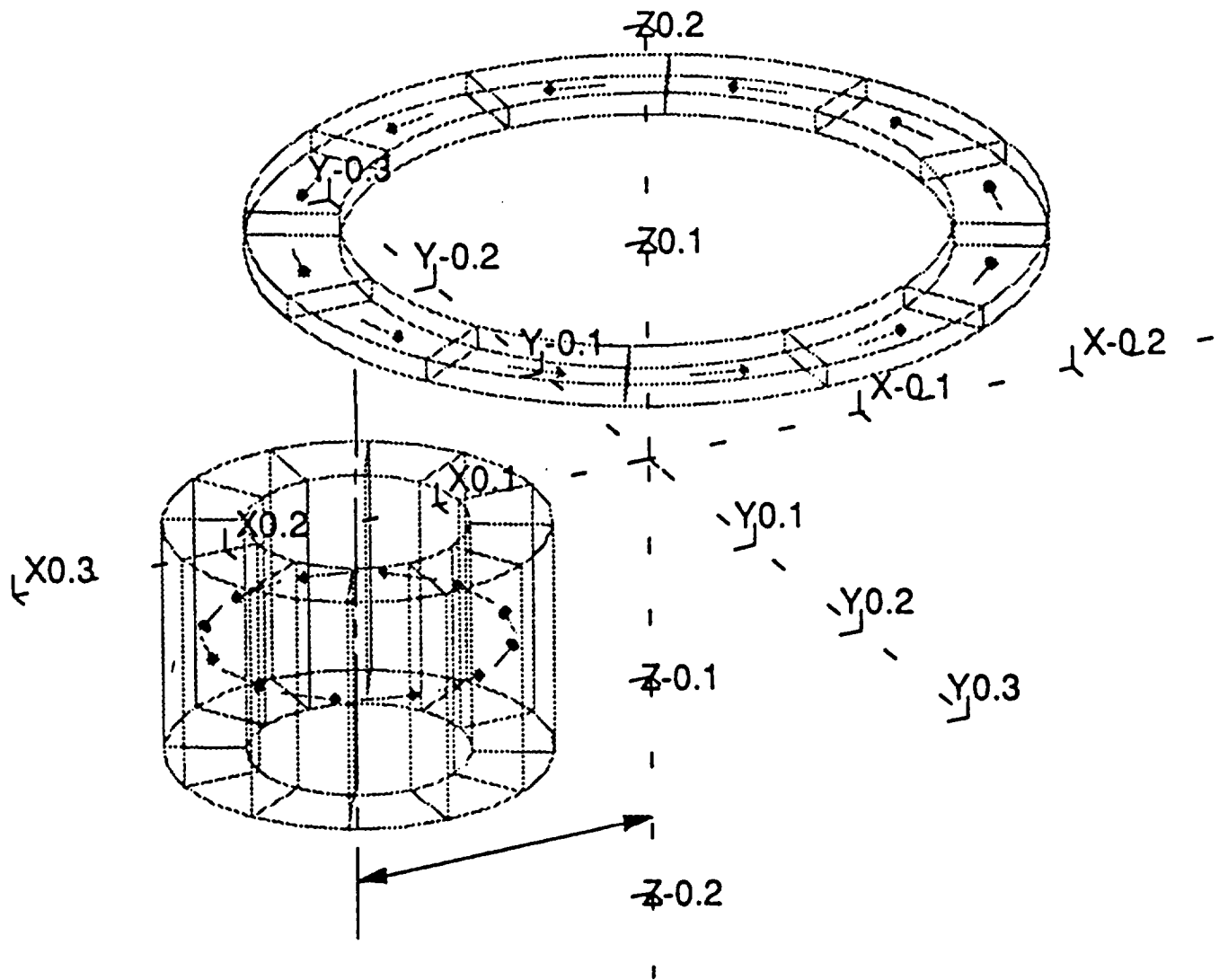


Figure 16 - Off-Axis Test Geometry

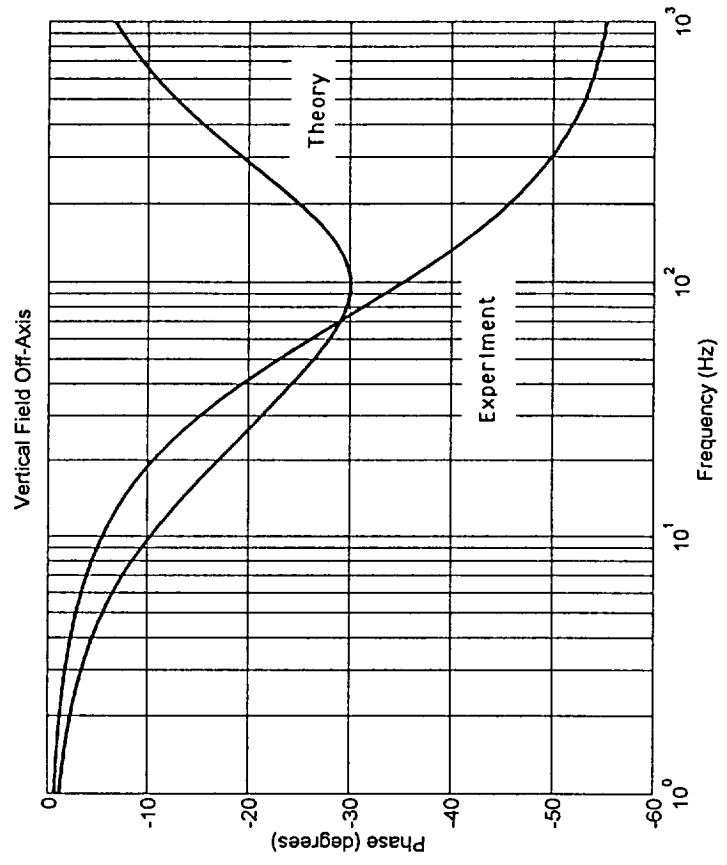
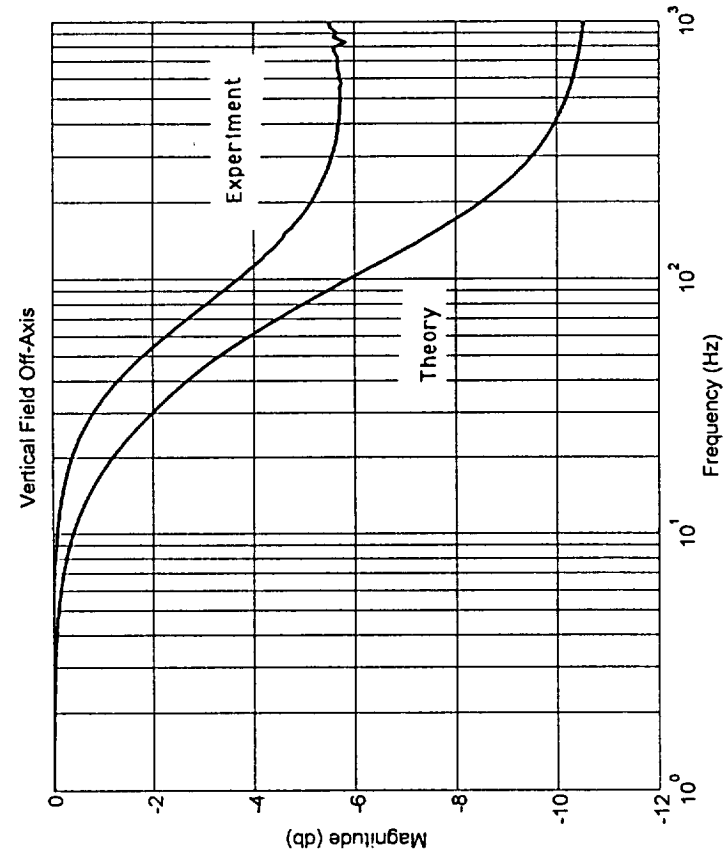


Figure 17 - Vertical Field with Off-Axis Test Set-Up

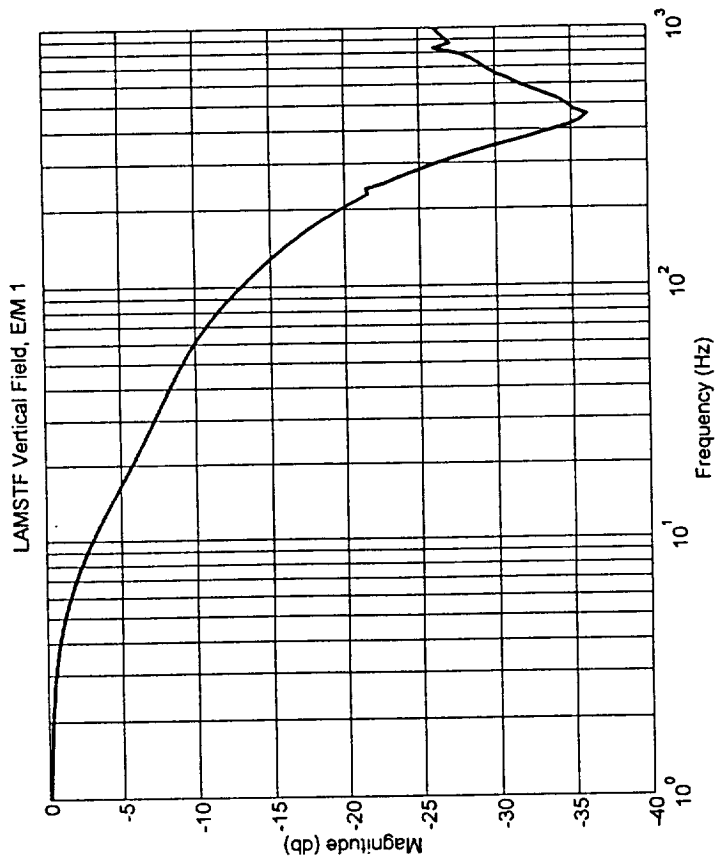
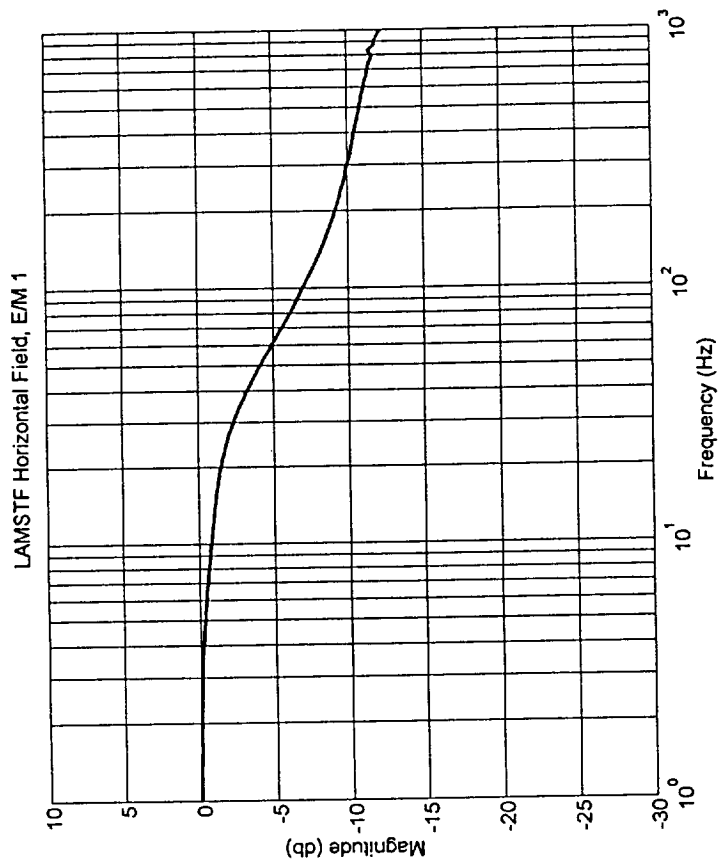


Figure 18 - Typical Field at Suspended Element with Full (Aluminum) Sensor Frame

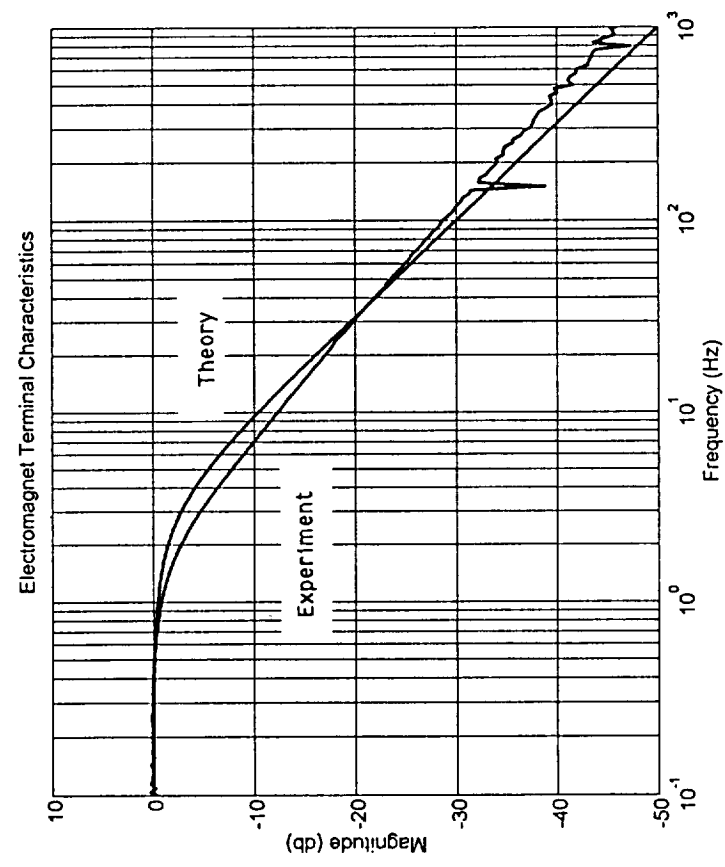
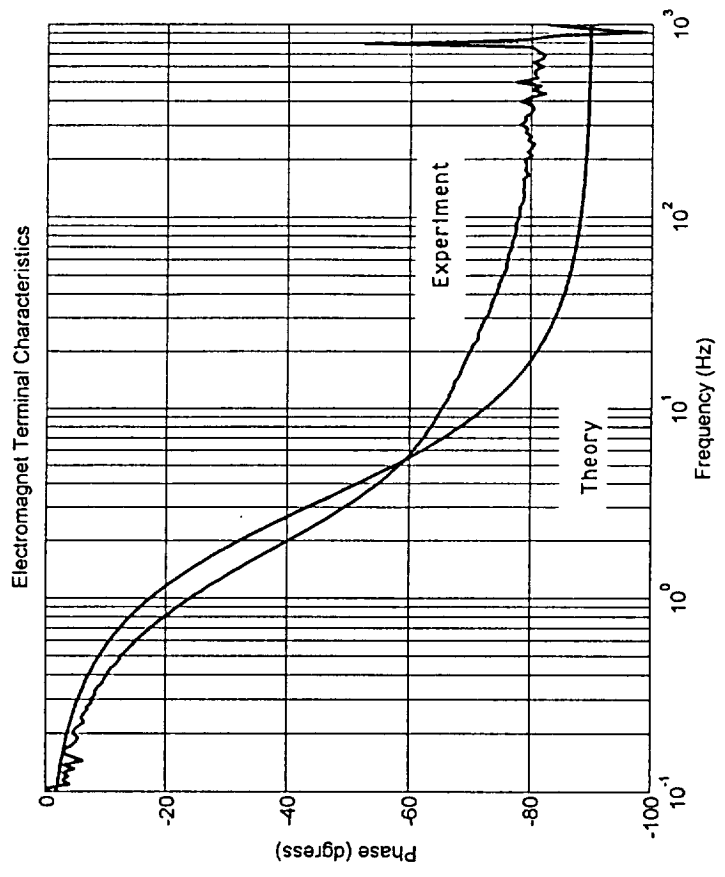


Figure 19 - Electromagnet Terminal Characteristics

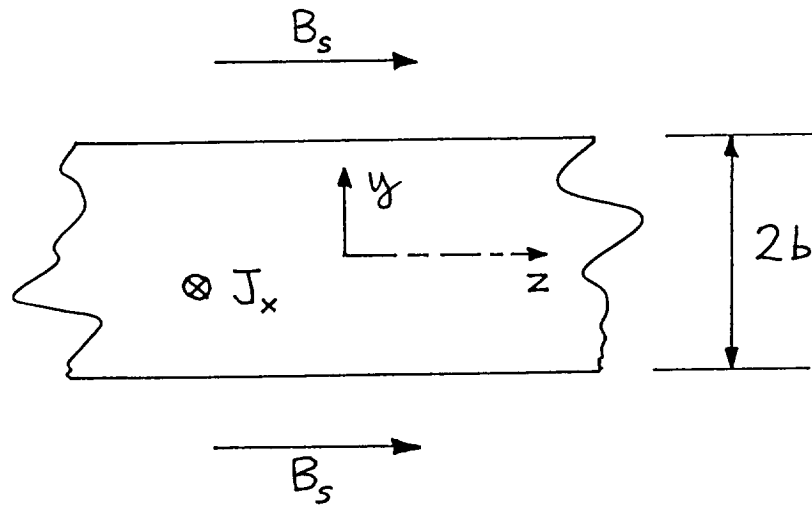


Figure 20 - Schematic of Infinite Flat Sheet Problem

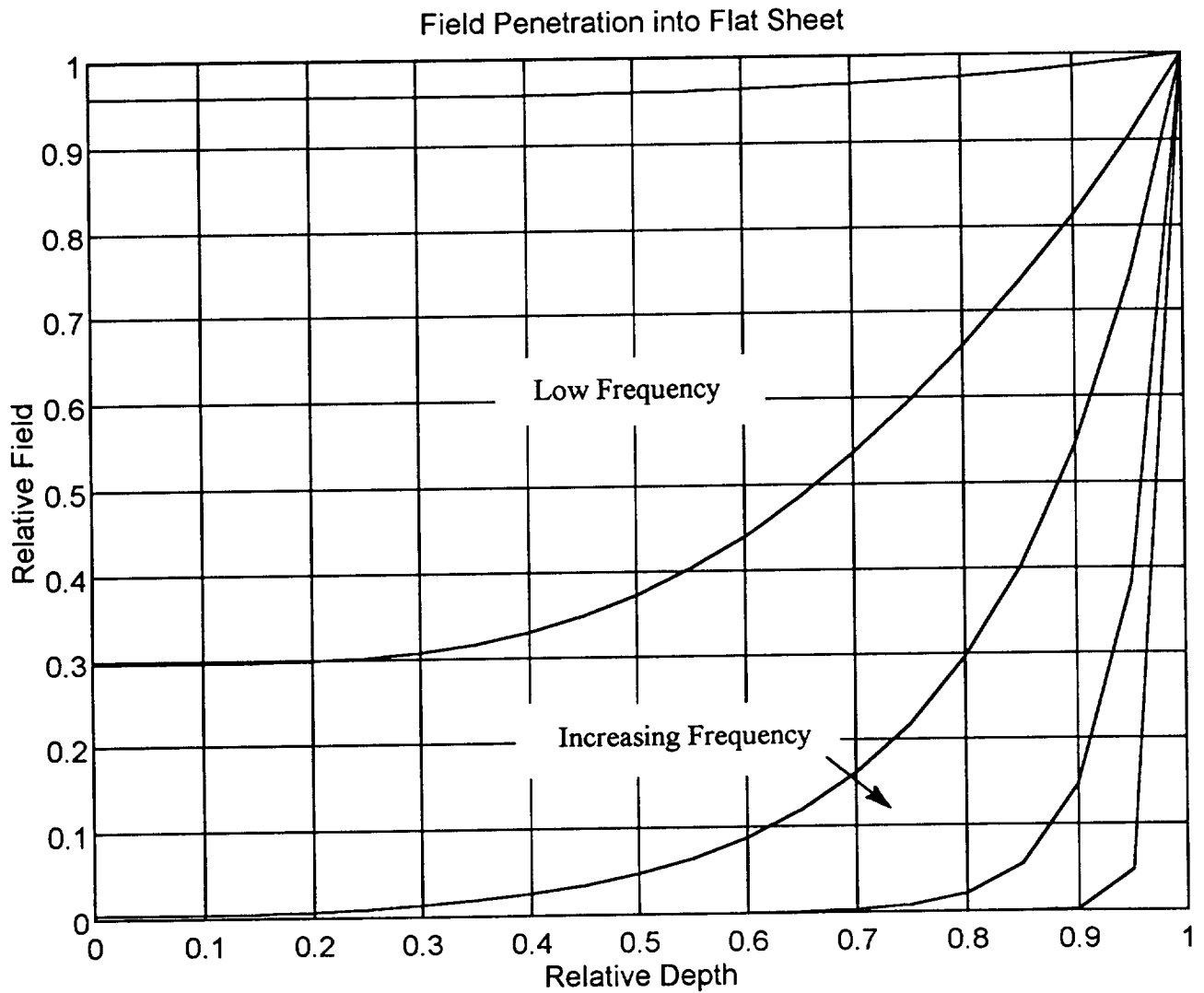


Figure 21 - Field Penetration for Infinite Flat Sheet Problem

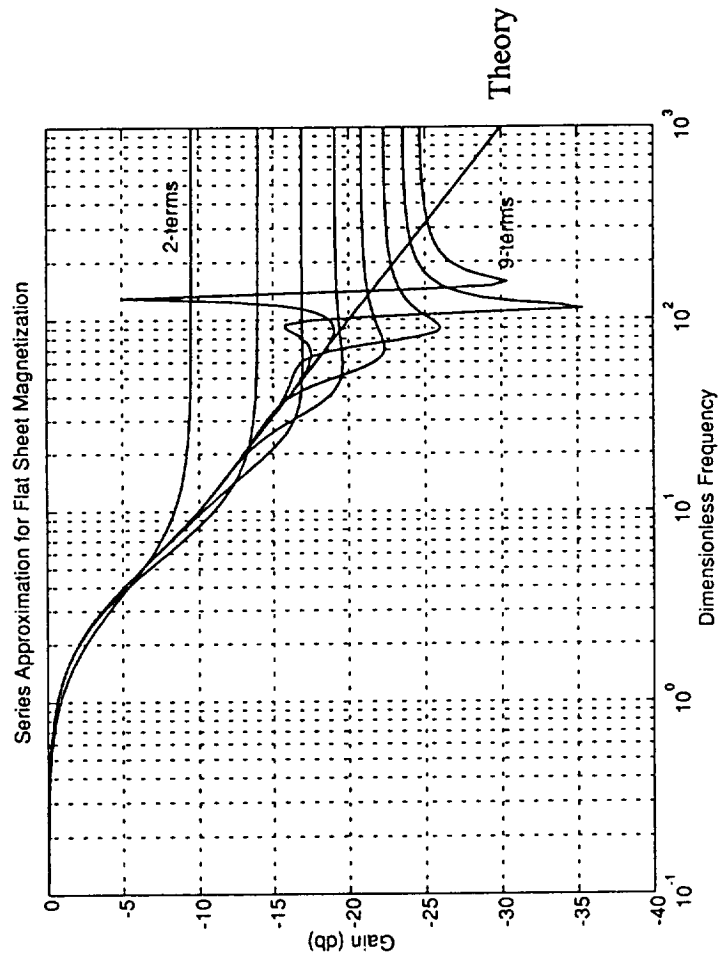
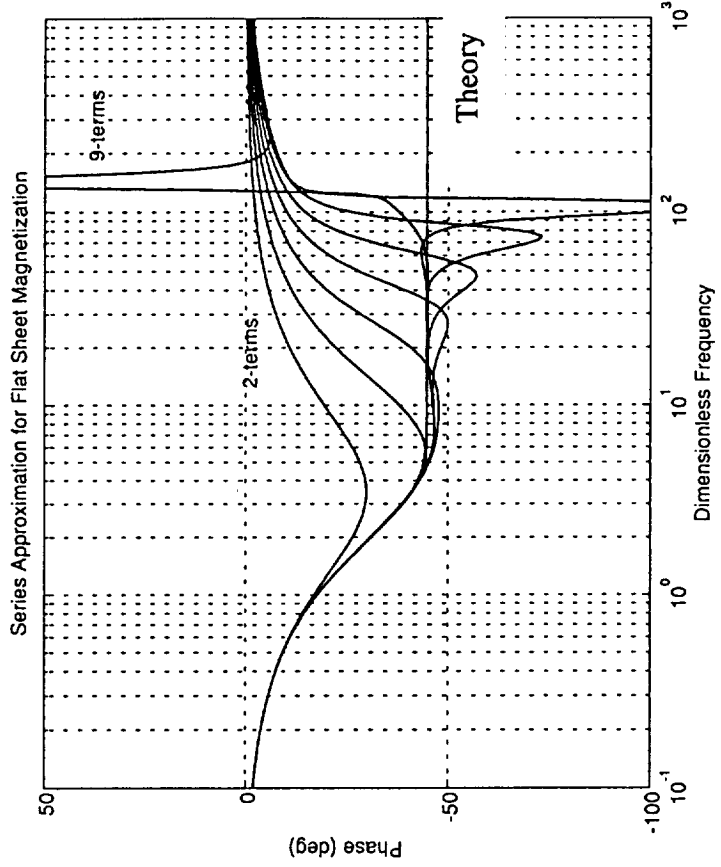


Figure 22 - Integrated Flux for Infinite Flat Sheet Problem

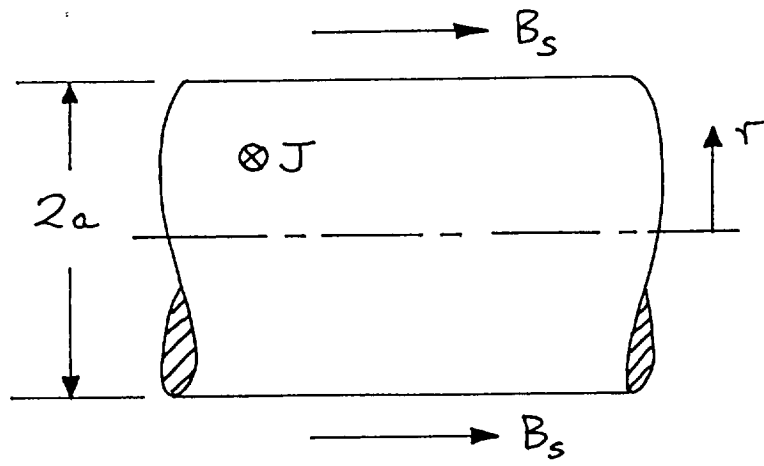


Figure 23 - Schematic of Infinite Cylindrical Bar Problem

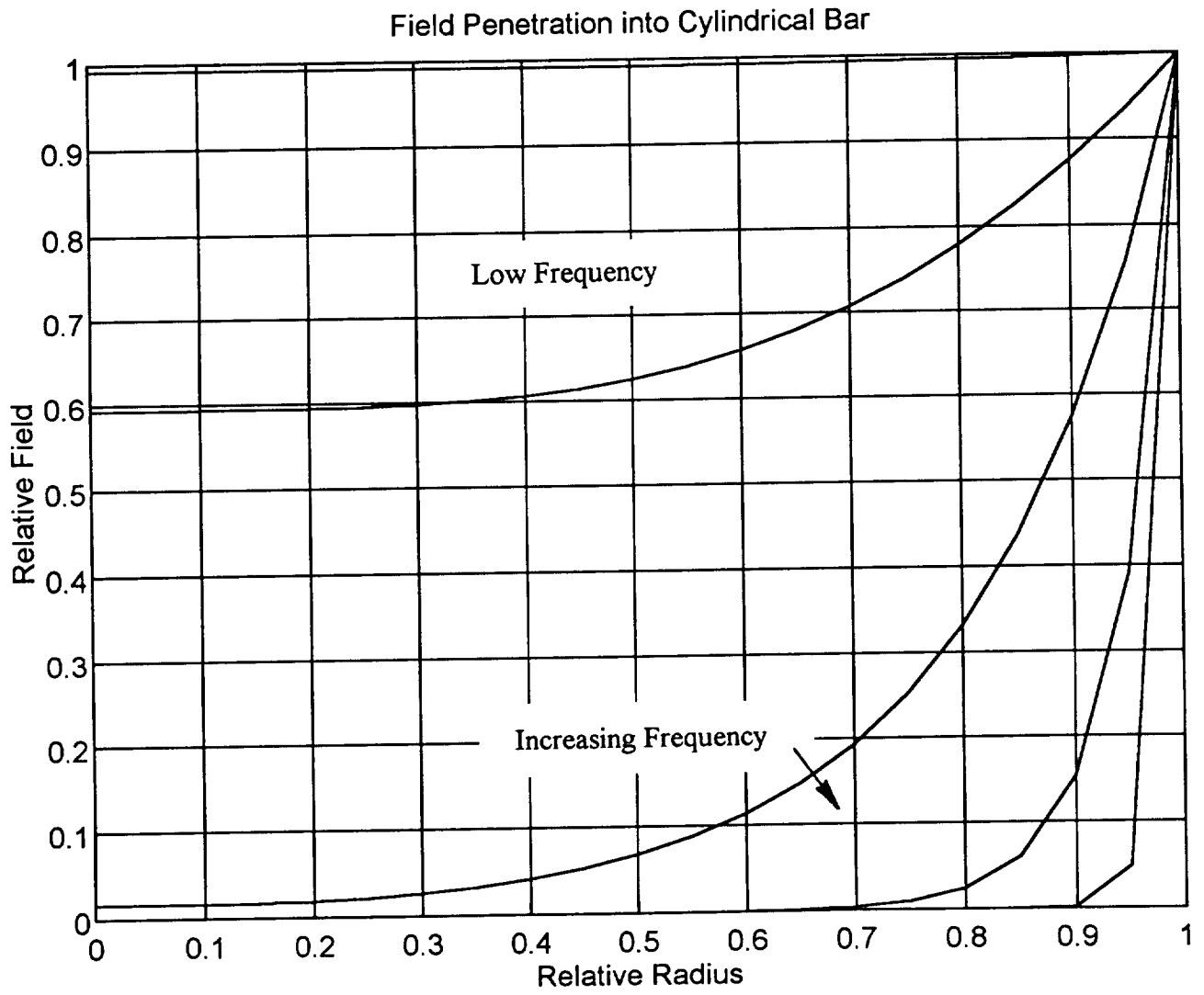


Figure 24 - Field Penetration for Infinite Cylindrical Bar Problem

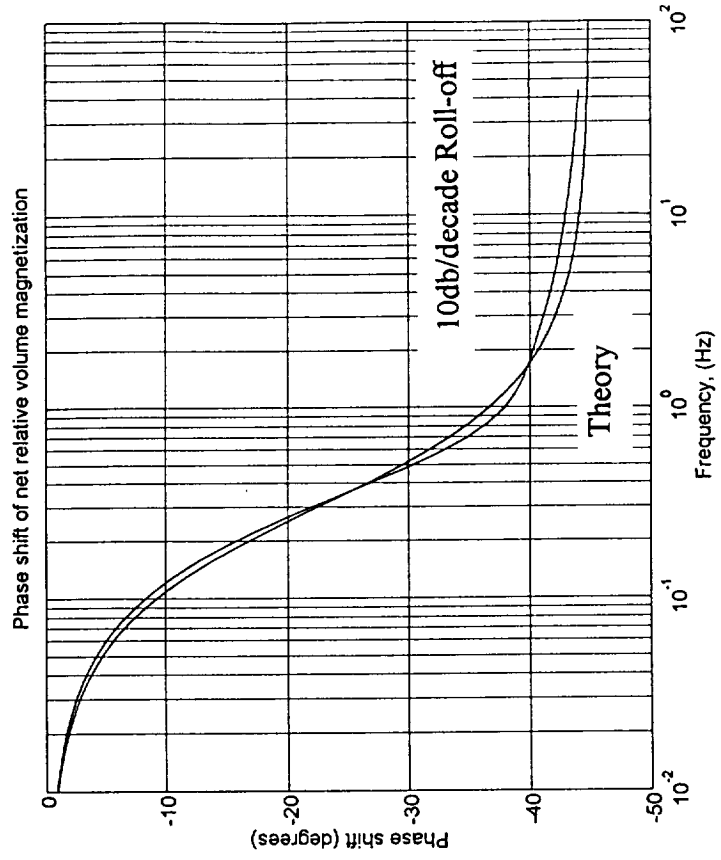
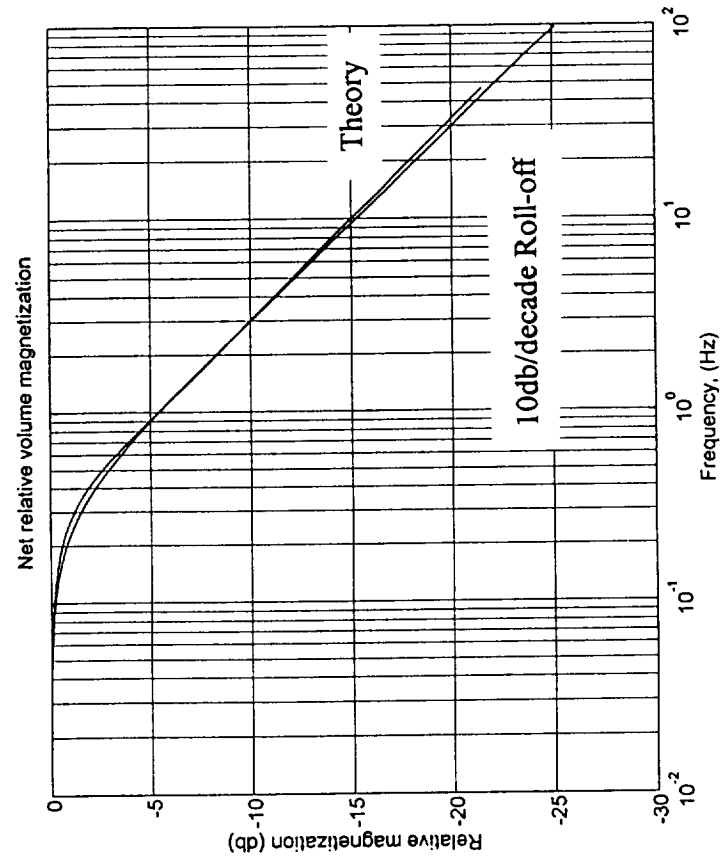


Figure 25 - Integrated Flux for Infinite Cylindrical Bar Problem

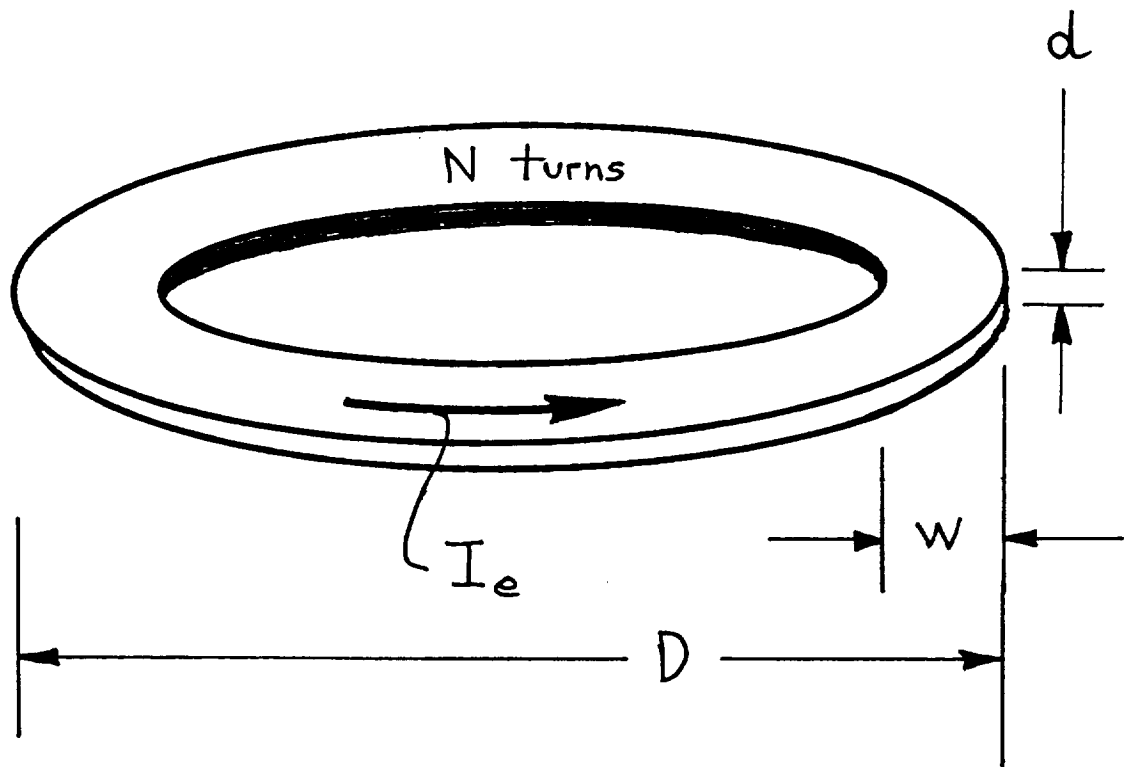


Figure 26 - Scaling Laws for Eddy Current Tests